Materials LAB

Research Article

CeO_2 Modified Ni-MOF as an Efficient Catalyst for Electrocatalytic Urea Oxidation

Xueting Wu[1,2], Lingling Li[1,2], Jing Pan[1], Xiao Wang[1,2*], Huabin Zhang[3], Shuyan Song[1,2*], and Hongjie Zhang[1,2,4*]

[1] *State Key Laboratory of Rare Earth Resource Utilization, Changchun Institute of Applied Chemistry, Chinese Academy of Sciences, Changchun 130022, China*
[2] *School of Applied Chemistry and Engineering, University of Science and Technology of China, Hefei 230026, China*
[3] *KAUST Catalysis Center (KCC), King Abdullah University of Science and Technology (KAUST), Thuwal, Saudi Arabia*
[4] *Department of Chemistry, Tsinghua University, Beijing 100084, China*
* Corresponding author, E-mail: wangxiao@ciac.ac.cn; songsy@ciac.ac.cn; hongjie@ciac.ac.cn

Abstract

The development of cost-efficient electrocatalysts for urea oxidation reaction (UOR) is a challenge due to the slow kinetics. In this work, we demonstrated a one-pot hydrothermal synthetic method to fabricate CeO_2 modified Ni-MOF nanosheets (NSs). When evaluted as UOR catalysts, the 3% CeO_2/Ni-MOF possesses outstanding catalytic activity, achieving the current density of 10 mA cm^{-2} at a low potential of 1.356 V with a small Tafel slope of 13.83 mV dec^{-1}. It is considered that the unique interactions between CeO_2 nanoparticles (NPs) and Ni-MOF NSs play the significant role in the enhancement of the catalytic performance by inducing the formation of abundant defects and optimized surface states.

Key words: CeO_2; electrocatalyst; Ni-MOFs; hybrid; UOR

Citation: Xueting Wu, Lingling Li, Jing Pan, Xiao Wang, Huabin Zhang, et al. CeO_2 Modified Ni-MOF as an Efficient Catalyst for Electrocatalytic Urea Oxidation. *Materials Lab* 2022, 1, 220009. DOI: 10.54227/mlab.20220009

1 Introduction

The electrocatalytic urea oxidation reaction (UOR) has shown tremendous potential in wastewater treatment and direct urea fuel cells.[1–8] More importantly, UOR is also an ideal alternative anode reaction to the conventional oxygen evolution reaction (OER, 1.23 V vs. RHE) in overall water-splitting to produce H_2 by its relatively low onset potential (0.37 V vs. RHE) in theory.[9–11] Although great progress has been made, UOR has hit a plateau in recent years, which can be attributed to the sluggish kinetics by the nature of the six-electron process.[11–14] Therefore, one of the center tasks in UOR is to develop high-performance catalysts for meeting the high requirements of practical applications.

Generally, noble metal-based catalysts, such as Pt- and Ru-based nanocomposites, possess high catalytic activity for UOR.[15–16] However, due to their scarcity and high cost, they are limited in current scientific research and commercialization.[17–18] Challenges remain in exploring cost-efficient catalysts composed of large-abundance elements to replace the precious noble metals. Recently, Ni-based materials such as $Ni(OH)_2$ and Ni-MOFs, have shown great potentials as UOR catalysts.[19–21] As a typical example, Wang et al. used NiZn-BTC as a self-sacrificial template to produce pomegranate-like Ni-doped carbon, which demonstrated the potential of 1.6 V at the current density of 10 mA cm^{-2} in UOR.[22] The unique performance of Ni-based catalysts is mainly from the in situ-formed Ni^{3+} species.[23–28] Despite these tremendous efforts, the activity and stability of the reported catalysts still have room for improvements, so it is urgent to develop an effective method to further enhance the catalytic performance.

It is widely considered that increasing the complexity in components and structures is a feasible route to upgrade the conventional catalysts.[27,29–34] That is because this combination can not only bring positive effects on catalytic performance due to the generation of strong interactions that do not belong to any of the counterparts, but also increase the contact opportunities of the reactants and the catalysts.[35] To date, many excellent progress has been achieved.[36–38] For example, Liu et al. developed Co_3O_4/CeO_2 nanohybrids, which reached an extremely low overpotential of 270 mV at the current density of 10 mA cm^{-2} in OER.[37] The incorporation of CeO_2 leads to more oxygen vacancies, which could strongly bind adsorbates and optimize the electronic structures, thus facilitating the turnover and transfer of the intermediates.[26,36–43] Inspired by these works, the combination of CeO_2 with Ni-based composites should be a viable way in UOR to tune the surface states of Ni-based composites to promote the catalytic performance. However, relatively few studies have been conducted in this regard, possibly owing to the lack of efficient ways to hybridize CeO_2 with Ni-based catalysts.

Following the above considerations, in this work, we employed ultrathin Ni-MOF nanosheets (NSs) with high specific

Received 24 February 2022; Accepted 6 March 2022; Published online

surface area as carriers to anchor CeO_2 nanoparticles (NPs) as promoters. Specifically, $Ni(OAc)_2{\cdot}4H_2O$, $Ce(NO_3)_3{\cdot}6H_2O$, and 1,4-BDC were mixed, followed by a one-pot hydrothermal process to produce the final products (Fig. 1a). When evaluated as UOR catalysts, the obtained 3% CeO_2/Ni-MOF shows remarkably enhanced catalytic activity, which only requires the potential of 1.356 V to achieve the current density of 10 mA cm^{-2} with a small Tafel slope of 13.83 mV dec^{-1}. Based on various characterizations, the significant role of CeO_2 can be mainly classified into three categories: the introduction of Ni^{3+} species, the promotion of electrochemical active surface area, and the optimization of electronic resistance.

2 Materials and methods

2.1 Chemicals

Nickel(II) acetate tetrahydrate ($Ni(OAc)_2{\cdot}4H_2O$), terephthalic acid (1,4-H_2BDC), Cerium nitrate hexahydrate ($Ce(NO_3)_3{\cdot}6H_2O$) were purchased from Aladdin; N,N-dimethylacetamide (DMAC) were purchased from Beijing Chemical Works. All materials were used without further purification.

2.2 Synthesis of Ni-MOF NSs with different CeO_2 contents

The synthesis of Ni-MOF NSs was carried out using a previously reported method.[26] In a typical synthesis of Ni-MOF NSs, an aqueous solution of $Ni(OAc)_2{\cdot}4H_2O$ (0.0248 g in 6 mL DI water) and a DMAC solution of 1,4-H_2BDC (0.0083 g in 6 mL DMAC) were added to a 20-mL Teflon vessel in sequence. The sealed vessel was transferred to a stainless steel autoclave and heated at 140 °C for 3 h. After cooling to room temperature, the precipitate was collected via centrifugation and washed with water and ethanol before drying for 12 h at 60 °C, denoted as Ni-MOF.

A similar experimental procedure was adopted for preparing other catalysts except adding $Ce(NO_3)_3{\cdot}6H_2O$ solution according to the atomic ratio of Ce : Ni of 1%, 3%, 5%, respectively denoted as 1% CeO_2/Ni-MOF, 3% CeO_2/Ni-MOF and 5% CeO_2/Ni-MOF.

2.3 Characterization

X-ray diffraction patterns were obtained on a Bruker D8 X-ray diffractometer with Cu Kα radiation (λ = 0.15418 nm). Transmission electron microscopic (TEM) images were obtained with a TECNAI G2 high-resolution transmission electron microscope, operating at 200 kV. The elemental compositions were analyzed by ICP-OES using a Varian Liberty 200 spectrophotometer. XPS measurement was performed on an ESCALAB-MKII 250 photoelectron spectrometer (VG Co.) with Al Kα X-ray radiation as the X-ray source for excitation. All samples were prepared by placing a drop of an ethanol suspension containing NSs onto the carbon-coated copper grids. Scanning electron microscopy (SEM) images and energy dispersive X-ray spectroscopy (EDS) were taken with a HITACHI S-4800 cold field-emission scanning electron microscope operated at 15 kV. FT-IR spectra (KBr pellets) were acquired with a Thermo Electron NEXUS 670 FT-IR spectrometer. Thermogravimetric analyses (TGA) were performed on a Mettler Toledo Star System under a nitrogen atmosphere at a heating rate of 10 °C min^{-1}. N_2 gas sorption experiments were carried out on the BELSORP-max (BEL, Japan).

2.4 Electrochemical measurements

Electrochemical measurements were made using a three-

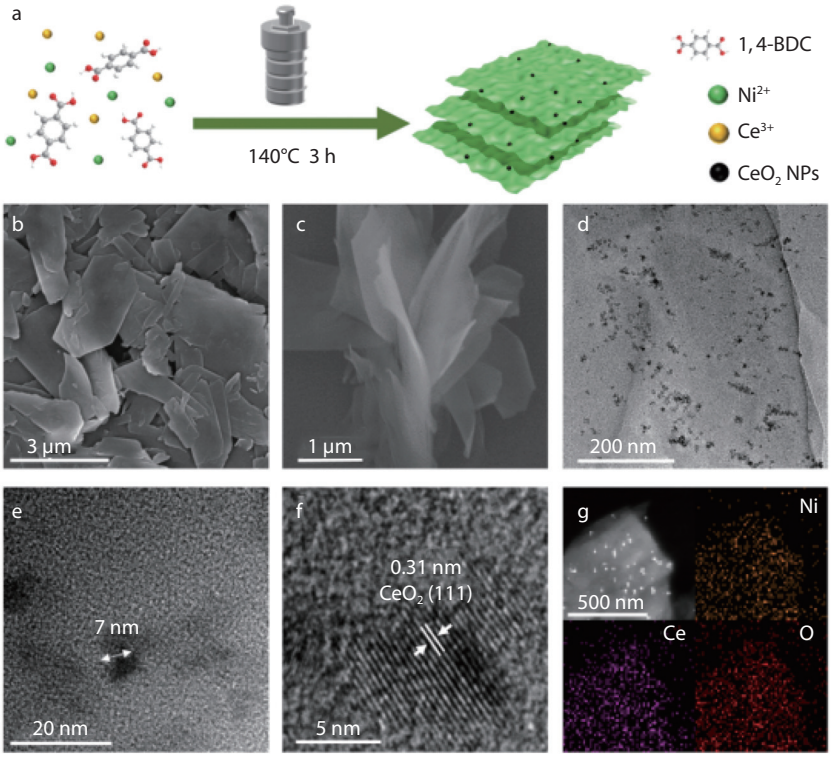

Fig. 1 (a) Schematic illustration of the formation of CeO_2/Ni-MOF. (b, c) SEM images, (d, e) TEM images, (f) HRTEM image and (g) elemental mapping images of 3% CeO_2/Ni-MOF.

DOI: 10.54227/mlab.20220009

electrode setup with a Hg/HgO (1 M KOH) electrode as the reference electrode and a Platinum electrode as the counter electrode, a glassy carbon (GC) disk electrode (3 mm in diameter) was used as the working electrode. The catalyst suspension was prepared by dispersing 5 mg catalyst containing 2.5 mg of catalyst and 2.5 mg carbon powder in 1 mL solution containing 500 μL deionized water, 470 μL ethanol and 30 μL 0.5 wt% Nafion solution followed by ultrasonication for 0.5 h. The above suspension (5 μL) was dropped onto the polished GC electrode and then dried at room temperature. Potentials were referenced to a reversible hydrogen electrode (RHE): $E_{RHE} = E_{Hg/HgO} + 0.098 + 0.059 \times pH$. 1 M KOH and 0.33 M urea solution was used as the electrolyte for urea oxidation reaction test.

Before data collection, the working electrodes were scanned by cyclic voltammetry (CV) plots until the signals were stabilized. The linear sweep voltammetry (LSV) curves were recorded with a scan rate of 5 mV s^{-1}. All data were corrected for iR loss unless otherwise noted. The chronopotentiometry was carried out under the same experimental setup without the iR drop compensation. Electrochemical impedance spectroscopy (EIS) was measured in the frequency range from 10 Hz to 100 mHz with an initial potential of 0.483 V. The electrical double layer capacitor (Cdl) was determined from cyclic voltammograms measured in a non-Faradaic region at different scan rates (v = 20, 40, 60, 80 and 100 mV s^{-1}) in the potential range 0.2 to 0.3 V versus Hg/HgO. The electrode durability was tested by Galvanostatic method, which was conducted at 10 mA cm^{-2} for 36000 s.

2.5 Calculation

Details concerning the calculation of mass activity and TOF are shown in the following:

The values of mass activity (A g^{-1}) were calculated from the Ni-MOF and CeO_2/Ni-MOF catalysts loading m (mg cm^{-2}) and the measured current density j (mA cm^{-2}) at η = 1.356 V

$$\text{Mass activity} = \frac{j}{m} \quad (1)$$

The values of TOF were calculated by assuming that every metal atom in the Ni-MOF and CeO_2/Ni-MOF catalysts was involved in the catalysis (lower TOF limits were calculated)

$$TOF = \frac{j \times S}{4 \times F \times n} \quad (2)$$

Here, j (mA cm^{-2}) is the measured current density at η = 1.356 V, S (cm^2) is the surface area of the electrode, the number 4 means four electrons per mole of O_2, F is Faraday's constant (96485.3 C mol^{-1}), and n is the moles of metal atom in the Ni-MOF and CeO_2/Ni-MOF catalysts on the electrode calculated from m and the molecular weight of the coated catalysts.

3 Results and Discussion

The specific synthetic steps are shown in Fig. 1a. We take 3% CeO_2/Ni-MOF as an example to investigate the structures of catalysts. The SEM images show that the sample has an obvious sheet-like morphology with longitudinal ultrathin characteristics (Fig. 1b and 1c). The TEM images confirm that the ateral size of the nanosheets is several microns with plenty of nanoparticles uniformly dispersed on the surface (Fig. 1d). The diameter of the nanoparticles is approximately 7 nm (Fig. 1e). The HRTEM images in Fig. 1f show that the nanoparticles have lattice spacing (d) of 0.31 nm, corresponding to the (111) crystallographic plane of CeO_2. The HAADF-STEM image and element mapping images demonstrate the uniform dispersion of Ni, Ce and O elements throughout the entire CeO_2/Ni-MOF (Fig. 1g). In Fig. 2a, the XRD shows that the patterns of all samples are in good agreement with those of Ni-MOF (JCPDS No.035-1677). And no signal is attributed to CeO_2. Notably, the peak intensity of Ni-MOF becomes weaker and weaker along with the increase of CeO_2 contents, indicating that the incorporation of CeO_2 destroys the crystallinity of Ni-MOF. Regarding the FT-IR spectra in Fig. 2b, the peak at 3588 cm^{-1} and the broad peaks between 3070 cm^{-1} and 3450 cm^{-1} are attributed to the stretching vibrations of -OH and water molecule, showing that there are coordinated -OH and H_2O in the samples. The absorption peak at 1502 cm^{-1} is attributed to the stretching vibration of the C-H group on the benzene ring. These two separated peaks at 1384 cm^{-1} and 1575 cm^{-1} are attributed to the asymmetric and symmetric vibrations of the coordinated carboxyl ($-COO^-$) group, which confirms that $-COO^-$ of 1,4-H_2BDC is coordinated with metal in a bidentate mode. The data of the FT-IR spectra matches well with the XRD results (Fig. 2a), suggesting the formation of Ni-MOF. All above the results firmly confirm the formation of CeO_2/Ni-MOF hybrid nanocompositions, which can be attributed to the stronger capability of Ce^{3+} ions in reacting with OH^- generated by the hydrolysis of CH_3COO^-, rather than coordinating with the ligands. Other samples with different CeO_2 contents were also studied, and the results reveal that they have similar morphological and structural characteristics, suggesting the structural robustness of the Ni-MOF NSs (Supporting Information, Figure S1-S4). In addition, 3% CeO_2/Ni-MOF also has similar trends of weightlessness to Ni-MOF in TGA (Supporting Information, Figure S5). These facts show that the incorporation of CeO_2 can not change the basic structure of the Ni-MOF. Moreover, the specific surface area of all samples remains nearly unchanged with the increase of CeO_2 contents, expressing that the specific surface area should not be the decisive factor towards the catalytic performance (Supporting Information, Table S1). According to the quantitative measurements by inductively coupled plasma-mass spectrometry (ICP-MS), the CeO_2 contents are 1.15%, 3.82%, 5.41%, which is nearly consistent with the feeding amounts. (Supporting Information, Figure S1-S4).

XPS was further employed to gain the information about the surface electronic states of the samples. As displayed in Fig. 2c, the Ni 2p spectrum mainly comprises two main peaks and two shakeup satellites (identified as Sat.). The peaks centered at 855.3 eV and 873.5 eV can be indexed to the Ni^{2+} ions, meanwhile the peaks located at 858.1 eV and 876.5 eV correspond to the local Ni^{3+} species. By integrating different components of Ni 2p spectrum, the ratio of Ni^{3+} to Ni^{2+} for 3% CeO_2/Ni-MOF is 0.29, while Ni-MOF has no Ni^{3+} species, suggesting Ni^{3+} species are formed due to the incorporation of CeO_2. Furthermore, compared with Ni-MOF, the peaks of Ni $2p_{3/2}$ and Ni $2p_{1/2}$ of the 3% CeO_2/Ni-MOF shift to a slightly lower binding energy (a shift of approximately 0.9 eV), which demonstrates the interaction between Ni and Ce. The Ce 3d spectrum is shown in Fig. 2d. The peaks at "U" and "V" corres-

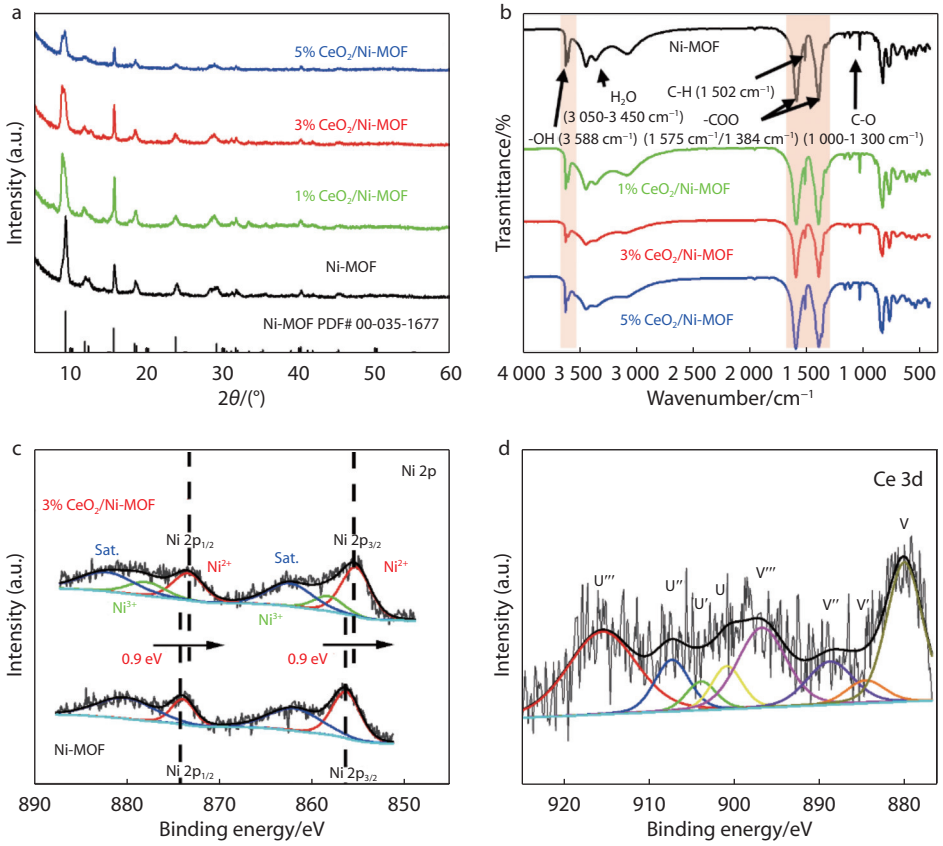

Fig. 2 (a) XRD patterns and (b) FT-IR spectra of different catalysts. (c) XPS Ni 2p spectra of Ni-MOF and 3% CeO_2/Ni-MOF. (d) XPS Ce 3d spectra of 3% CeO_2/Ni-MOF.

pond to Ce $3d_{3/2}$ and Ce $3d_{5/2}$ of CeO_2. The doublets (V, U), (V″, U″) and (V‴, U‴) are identified as the different states of Ce^{4+} species, while the doublets (V′, U′) are identified as the Ce^{3+} ions.[44] The intensity of peaks is weak due to the low Ce contents, but it still can be seen that the majorities of the Ce elements are present in +4 valence. The XPS spectra of other catalysts are similar to 3% CeO_2/Ni-MOF (Supporting Information, Figure S6-S9). All of the foregoing findings show that CeO_2-modified Ni-MOF NSs are successfully manufactured.

To evaluate the catalytic performance of CeO_2/Ni-MOF catalysts for UOR, a series of electrochemical measurements were carried out using a three-electrode configuration. The electrocatalytic properties are all measured by depositing catalysts on a glassy carbon electrode. As shown in Fig. 3a, we first conducted the OER test in 1M KOH without urea. The 3% CeO_2/Ni-MOF requires a potential of 1.557 V vs RHE at the current density of 10 mA cm^{-2}. After adding 0.33 M urea into 1 M KOH, the polarization curve becomes very steep, and the 3% CeO_2/Ni-MOF only requires a potential of 1.356 V vs RHE at the current density of 10 mA cm^{-2}, which is 201 mV lower than OER. The above results indicate that the UOR is successfully triggered (Fig. 3a). In order to investigate the composition effects, we further tested the LSV curves of the obtained Ni-MOF, CeO_2 and CeO_2/Ni-MOF hybrids with different CeO_2 contents (Fig. 3b and 3d). The potential at the current density 10 mA cm^{-2} follows such a sequence: 3% CeO_2/Ni-MOF (1.356 V) < 5% CeO_2/Ni-MOF (1.369 V) < 1% CeO_2/Ni-MOF (1.373 V) < Ni-MOF (1.385 V) < CeO_2 NPs (~1.475 V), clearly demonstrating the superiority of the 3% CeO_2/Ni-MOF catalyst. In addition, the Tafel slope was also calculated. The 3% CeO_2/Ni-MOF has the lowest value of 13.83 mV dec^{-1} among these samples, indicating its faster UOR kinetics (Fig. 3c). The mass activity and TOF for these electrodes are in the same sequence at the potential of 1.356 V (Fig. 3e and 3f). The sequence is as follows: 3% CeO_2/Ni-MOF (15.56 A g^{-1} and 0.02822 s^{-1}) > 5% CeO_2/Ni-MOF (4.23 A g^{-1} and 0.00768 s^{-1}) > 1% CeO_2/Ni-MOF (3.41 A g^{-1} and 0.00617 s^{-1}) > Ni-MOF (2.07 A g^{-1} and 0.00375 s^{-1}). Sequentially, we performed the double-layer capacitance (Cdl) analyses to compare the electrochemical active surface area (ECSA) measured by cyclic voltammograms (CVs).[45] The CVs with different scan rates are in the potential range of 0.2-0.3 V to obtain the capacitive current for Ni-MOF, 1% CeO_2/Ni-MOF, 3% CeO_2/Ni-MOF and 5% CeO_2/Ni-MOF (Supporting Information, Figure S10), then the Cdl was calculated by plotting $\Delta j = j_a - j_c$ at 0.25 V as shown in Fig. 3g. The linear slopes follow the same sequence of mass activity and TOF: 3% CeO_2/Ni-MOF (2.32 mF cm^{-2}) > 5% CeO_2/Ni-MOF (1.59 mF cm^{-2}) > 1% CeO_2/Ni-MOF (1.25 mF cm^{-2}) > Ni-MOF (1.23 mF cm^{-2}), implying that the remarkable UOR activity of the 3% CeO_2/Ni-MOF is relevant to the largest electrochemical active surface area. Moreover, the Nyquist plots derived from the electrochemical impedance spectroscopy (EIS) are shown in Fig. 3h and Table S2. The semicircle diameter of the 3% CeO_2/Ni-MOF is much smaller than those of others. Therefore, the low resistance is considered as another key factor in the improved UOR performance of the 3% CeO_2/Ni-MOF. Not-

DOI: 10.54227/mlab.20220009

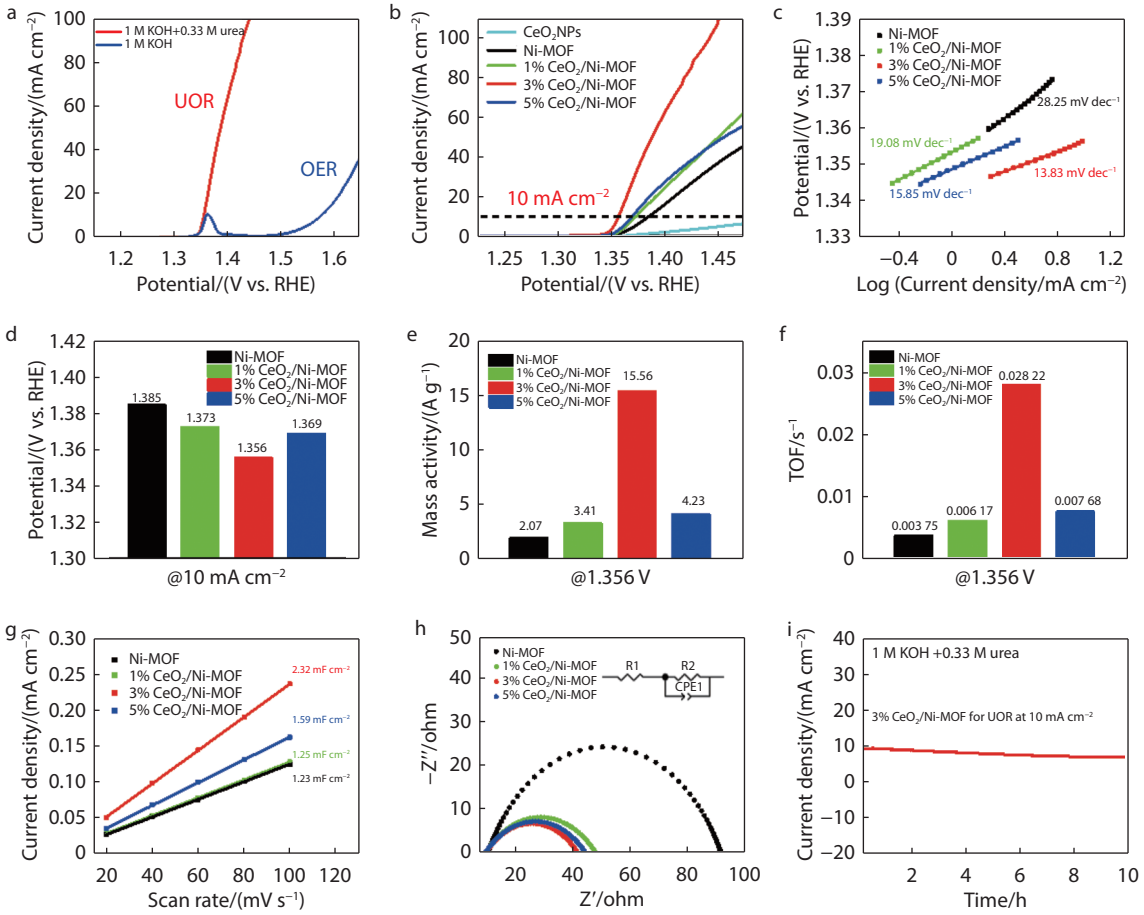

Fig. 3 (a) LSV curves of 3% CeO_2/Ni-MOF in 1 M KOH electrolyte with and without 0.33 M urea. (b) LSV curves of CeO_2 NPs, Ni-MOF, 1% CeO_2/Ni-MOF, 3% CeO_2/Ni-MOF and 5% CeO_2/Ni-MOF in 1 M KOH electrolyte with 0.33 M urea. (c) Tafel plots, (d) potentials at 10 mA cm^{-2}, (e) mass activity at η = 1.356 V, (f) TOF at η = 1.356 V, (g) current density differences at 0.25 V plotted against scan rate in a non-Faradaic and (h) Nyquist plots recorded at 0.483 V of Ni-MOF, 1% CeO_2/Ni-MOF, 3% CeO_2/Ni-MOF and 5% CeO_2/Ni-MOF. (i) Chronopotentiometry curves of 3% CeO_2/Ni-MOF at 10 mA cm^{-2}.

ably, though the introduction of CeO_2 can enhance the catalytic activity of the MOF, bare CeO_2 exhibits poor UOR activity, and the increase of CeO_2 contents will induce the difficulty in mass and electron transfer. Therefore, 3% CeO_2/Ni-MOF is considered reaching the balance between mass/electron transfer and specific active sites. Further increase or decrease the CeO_2 contents will cause the decrease in UOR activity.

Besides the large electrochemical active surface area and small electronic resistance, the presence of a high concentration of Ni^{3+} species is also of great significance towards the catalytic performance. Previous reports reveal that Ni^{3+} species possess higher UOR activity compared with Ni^{2+} species.[9,23–24] That is because Ni^{3+} species possess much stronger capabilities of binding adsorbates and accepting electrons, which could greatly accelerate the mass and charge transfer.[20,25,33,46] As aforementioned, the XPS results clearly demonstrate that the addition of CeO_2 can enhance the contents of Ni^{3+} species (Fig. 2c). Therefore, we believed that these Ni^{3+} ions efficiently promote the catalytic process. In brief, the reasons for enhancements can be mainly classified into three categories: the presence of high amount of Ni^{3+} species, the larger electrochemical active surface area, and the smaller electronic resistance.

Finally, a galvanostatic experiment for 3% CeO_2/Ni-MOF was performed at the constant current density of 10 mA cm^{-2} for 10 h. As shown Fig. 3i, the current density of 3% CeO_2/Ni-MOF decreases slightly over 36000 s. After that, we measured the LSV of the catalyst, and found that the catalytic activity did have a declining trend (Supporting Information, Figure S11d). In order to explore the reasons for the decrease of activity, we monitored the changes of 3% CeO_2/Ni-MOF during the reaction. As shown in Figure S11a, the initial sheet-like structures are well maintained after 50-cycles activation. After an hour, a few amorphous structures are observed apart from the nanosheets (Figure S11b and S11c). The corresponding XRD patterns reveal that the peak intensity of Ni-MOF becomes weaker and weaker, meanwhile the peak intensity of $Ni(OH)_2$ rises gradually (Fig. 4). Two hours later, the signals belonging to Ni-MOF disappeared completely, indicating the occurrence of phase transition, which can be attributed to the unstability of Ni-MOFs in alkali solution. The signal around 26° can be assigned to the diffraction peak of the residual carbon paper introduced during the collection process. Therefore, we concluded here that CeO_2/Ni-MOF has higher UOR activity than CeO_2/$Ni(OH)_2$, owing to the presence of Ni^{3+} species. However, along with the reaction going, $Ni(OH)_2$ is generated

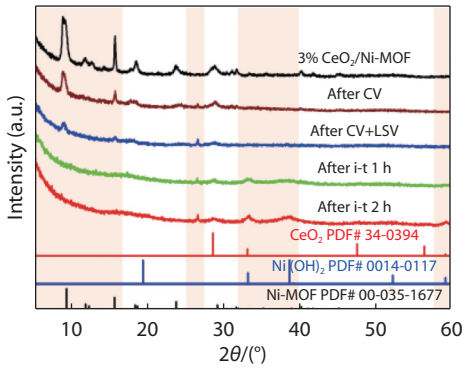

Fig. 4 XRD patterns of 3% CeO_2/Ni-MOF during UOR process.

with the continually decreased Ni^{3+} content. It well explains the slight activity lose during the galvanostatic test. When Ni-MOF decomposed completely, the activity fianlly stabilized as shown in Fig. 3i.

4 Conclusions

In summary, we demonstrated a one-pot hydrothermal synthetic method to fabricate CeO_2 modified Ni-MOF nanosheets. The obtained 3% CeO_2/Ni-MOF shows remarkably enhanced activity, achieving the current density of 10 mA cm^{-2} at a low potential of 1.356 V with a small Tafel slope of 13.83 mV dec^{-1}. It is considered that CeO_2 can regulate the electronic structures of the metal sites on the surface of Ni-MOF NSs, thus improving the electrocatalytic activity. We believed that the as-developed route by incorporating CeO_2 as promoters will pave a new way for upgrading the catalytic performance of conventional catalysts in a wide range of energy-relied applications.

Acknowledgments

This work was supported by the financial aid from the National Natural Science Foundation of China (Grant No.21771173, 22020102003 and 22025506), National Key Research and Development Program of China (2021YFB3500703, 2016YFA0203200), and K. C. Wong Education Foundation (GJTD-2018-09).

Conflict of interest

The authors declare no conflict of interest.

Author contributions

X. Wang, S. Y. Song and H. J. Zhang proposed the research direction and guided the project. X. Wang and X. T. Wu designed and performed the experiments. X. T. Wu, X. Wang and S. Y. Song analyzed and discussed the experimental results and drafted the manuscript. X. T. Wu, L. L. Li, J. Pan, X. Wang and H. B. Zhang joined the discussion of data and gave useful suggestions.

REFERENCES

1. X. J. Zhu, X. Y. Dou, J. Dai, X. D. An, Y. Q. Guo, L. D. Zhang, S. Tao, J. Y. Zhao, W. S. Chu, X. C. Zeng, C. Z. Wu, Y. Xie, *Angew. Chem. Int. Ed.*, 2016, 55, 12465
2. Y. B. Li, C. Zhong, J. Liu, X. Q. Zeng, S. X. Qu, X. Han, Y. P. Deng, W. B. Hu, J. Lu, *Adv. Mater.*, 2018, 30, 1703657
3. N. Senthilkumar, G. G. Kumar, A. Manthiram, *Adv. Energy. Mater.*, 2018, 8, 1702207
4. J. Y. Zhang, T. He, M. Wang, R. Qi, Y. Yan, Z. Dong, H. Liu, H. Wang, B. Y. Xia, *Nano Energy*, 2019, 60, 894
5. S. J. Yao, S. K. Wolfson, B. K. Ahn, C. C. Liu, *Nature*, 1973, 241, 471
6. Z. L. Wang, W. J. Liu, Y. M. Hu, M. L. Guan, L. Xu, H. P. Li, J. Bao, H. M. Li, *Appl. Catal. B*, 2020, 272, 118959
7. H. C. A. Sun, W. Zhang, J. G. Li, Z. S. Li, X. Ao, K. H. Xue, K. K. Ostrikov, J. Tang, C. D. Wang, *Appl. Catal. B*, 2021, 284, 119740
8. N. Wu, R. H. Guo, X. Zhang, N. Gao, X. Y. Chi, D. L. Cao, T. P. Hu, *J. Alloys Compd.*, 2021, 870, 159408
9. L. P. Wang, Y. J. Zhu, Y. Z. Wen, S. Y. Li, C. Y. Cui, F. L. Ni, Y. X. Liu, H. P. Lin, Y. Y. Li, H. S. Peng, B. Zhang, *Angew. Chem. Int. Ed.*, 2021, 60, 10577
10. H. Jiang, M. Sun, S. Wu, B. Huang, C. S. Lee, W. Zhang, *Adv. Funct. Mater.*, 2021, 31, 2104951
11. L. Xia, Y. Liao, Y. Qing, H. Xu, Z. Gao, W. Li, Y. Wu, *ACS Appl. Energy Mater.*, 2020, 3, 2996
12. B. Zhu, Z. Liang, R. Zou, *Small*, 2020, 16, 1906133
13. S. Chen, J. J. Duan, A. Vasileff, S. Z. Qiao, *Angew. Chem. Int. Ed.*, 2016, 55, 3804
14. X. Zhang, Y. Y. Liu, Q. Z. Xiong, G. Q. Liu, C. J. Zhao, G. Z. Wang, Y. X. Zhang, H. M. Zhang, H. J. Zhao, *Electrochim. Acta*, 2017, 254, 44
15. Z. W. Seh, J. Kibsgaard, C. F. Dickens, I. B. Chorkendorff, J. K. Norskov, T. F. Jaramillo, *Science*, 2017, 355, eaad4998
16. M. P. Browne, Z. Sofer, M. Pumera, *Energy Environ. Sci.*, 2019, 12, 41
17. H. Liu, S. Zhu, Z. Cui, Z. Li, S. Wu, Y. Liang, *Nanoscale*, 2021, 13, 1759
18. G. Yang, Y. Jiao, H. Yan, C. Tian, H. Fu, *Small Struct.*, 2021, 2, 2100095
19. J. Xie, L. Gao, S. Cao, W. Liu, F. Lei, P. Hao, X. Xia, B. Tang, *J. Mater. Chem. A*, 2019, 7, 13577
20. D. D. Zhu, C. X. Guo, J. L. Liu, L. Wang, Y. Dub, S. Z. Qiao, *Chem. Commun.*, 2017, 53, 10906
21. J. F. Xie, W. W. Liu, F. C. Lei, X. D. Zhang, H. C. Qu, L. Gao, P. Hao, B. Tang, Y. Xie, *Chem. Eur. J.*, 2018, 24, 18408
22. L. Wang, L. Ren, X. Wang, X. Feng, J. Zhou, B. Wang, *ACS Appl. Mater. Inter.*, 2018, 10, 4750
23. L. S. Zhang, L. P. Wang, H. P. Lin, Y. X. Liu, J. Y. Ye, Y. Z. Wen, A. Chen, L. Wang, F. L. Ni, Z. Y. Zhou, S. G. Sun, Y. Y. Li, B. Zhang, H. S. Peng, *Angew. Chem. Int. Ed.*, 2019, 58, 16820
24. D. A. Daramola, D. Singh, G. G. Botte, *J. Phys. Chem. A*, 2010, 114, 11513
25. F. P. Cheng, Z. J. Li, L. Wang, B. Yang, J. G. Lu, L. C. Lei, T. Y. Ma, Y. Hou, *Mater. Horiz.*, 2021, 8, 556
26. F. L. Li, P. T. Wang, X. Q. Huang, D. J. Young, H. F. Wang, P. Braunstein, J. P. Lang, *Angew. Chem. Int. Ed.*, 2019, 58, 7051
27. K. Rui, G. Zhao, Y. Chen, Y. Lin, Q. Zhou, J. Chen, J. Zhu, W. Sun, W. Huang, S. X. Dou, *Adv. Funct. Mater.*, 2018, 28, 1801554
28. Y. Tong, P. Z. Chen, M. X. Zhang, T. P. Zhou, L. D. Zhang, W. S. Chu, C. Z. Wu, Y. Xie, *ACS Catal.*, 2018, 8, 1
29. F. L. Li, Q. Shao, X. Huang, J. P. Lang, *Angew. Chem. Int. Ed.*, 2018, 57, 1888
30. T. Y. Kou, S. W. Wang, J. L. Hauser, M. P. Chen, S. R. J. Oliver, Y. F. Ye, J. H. Guo, Y. Li, *ACS Energy Lett.*, 2019, 4, 622
31. W. C. Records, Y. Yoon, J. F. Ohmura, N. Chanut, A. M. Belcher, *Nano Energy*, 2019, 58, 167
32. X. L. Chen, X. Zhong, B. W. Yuan, S. Q. Li, Y. B. Gu, Q. Q. Zhang, G. L. Zhuang, X. N. Li, S. W. Deng, J. G. Wang, *Green Chem.*, 2019, 21, 578
33. Y. Zhai, X. Ren, J. Yan, S. Liu, *Small Struct.*, 2021, 2, 2000096

DOI: 10.54227/mlab.20220009

34. L. N. Sha, K. Ye, G. Wang, J. Q. Shao, K. Zhu, K. Cheng, J. Yan, G. L. Wang, D. X. Cao, *Chem. Eng. J.*, 2019, 359, 1652
35. H. Xu, Z.-X. Shi, Y.-X. Tong, G.-R. Li, *Adv. Mater.*, 2018, 30, 1703657
36. G. L. Lu, H. Y. Zheng, J. J. Lv, G. Wang, X. B. Huang, *J. Power Sources*, 2020, 480, 229091
37. Y. Liu, C. Ma, Q. Zhang, W. Wang, P. Pan, L. Gu, D. Xu, J. Bao, Z. Dai, *Adv. Mater.*, 2019, 31, 1900062
38. D. D. Zhao, Y. C. Pi, Q. Shao, Y. G. Feng, Y. Zhang, X. Q. Huang, *ACS Nano*, 2018, 12, 6245
39. J. Yu, Q. Cao, Y. Li, X. Long, S. Yang, J. K. Clark, M. Nakabayashi, N. Shibata, J. J. Delaunay, *ACS Catal.*, 2019, 9, 1605
40. X. J. Feng, Y. L. Shi, Y. S. Wang, S. X. Min, Z. A. Hu, *Chin. J. Appl. Chem.*, 2011, 28, 302
41. D. Y. Liu, N. W. Yang, Q. Zeng, H. Liu, D. Chen, P. L. Cui, L. Xu, C. Q. Hu, J. Yang, *Chin. Chem. Lett.*, 2021, 32, 3288
42. J. H. Kim, K. Shin, K. Kawashima, D. H. Youn, J. Lin, T. E. Hong, Y. Liu, B. R. Wygant, J. Wang, G. Henkelman, C. B. Mullins, *ACS Catal.*, 2018, 8, 4257
43. W. Gao, Z. Xia, F. Cao, J. C. Ho, Z. Jiang, Y. Qu, *Adv. Funct. Mater.*, 2018, 28, 1870071
44. L. L. Zhang, J. Pan, Y. Long, J. Li, W. Li, S. Y. Song, Z. Shi, H. J. Zhang, *Small*, 2019, 15, 1903182
45. L. N. Sha, J. L. Yin, K. Ye, G. Wang, K. Zhu, K. Cheng, J. Yan, G. L. Wang, D. X. Cao, *J. Mater. Chem. A*, 2019, 7, 9078
46. J. P. Li, G. B. Zhao, H. Y. Zhao, N. N. Zhao, L. L. Lu, N. L. Liu, M. Wang, C. J. Ma, Q. Zhang, Y. P. Du, *Nanoscale*, 2021, 13, 3581
47. G. Ma, Q. Xue, J. Y. Zhu, X. Y. Zhang, X. Wang, H. C. Yao, G. F. Zhou, Y. Chen, *Appl. Catal. B*, 2020, 265, 118567
48. Z. Li, M. Shao, L. Zhou, R. Zhang, C. Zhang, M. Wei, D. G. Evans, X. Duan, *Adv. Mater.*, 2016, 28, 2337
49. G. Chakraborty, I. H. Park, R. Medishetty, J. J. Vittal, *Chem. Rev.*, 2021, 121, 3751
50. S. Dang, Q. L. Zhu, Q. Xu, *Nat. Rev. Mater.*, 2018, 3, 17075
51. T. V. M. Sreekanth, G. R. Dillip, P. C. Nagajyothi, K. Yoo, J. Kim, *Appl. Catal. B*, 2021, 285, 119793